PNAS RESEARCH ARTICLE | ENGINEERING

Self-healing for the long haul: In situ automation delivers century-scale fracture recovery in structural composites

Jack S. Turicek[a], Zachary J. Phillips[b], Kalyana B. Nakshatrala[c], and Jason F. Patrick[a,b,1]

Affiliations are included on p. 8.

Edited by David Weitz, Harvard University, Cambridge, MA; received September 1, 2025; accepted November 24, 2025

Nature's structural composites, such as bone and wood, achieve mechanical performance through hierarchical multimaterial design. Though, their real vantage lies in the exceptional ability to repeatedly heal after damage. Synthetic fiber-reinforced polymer (FRP) composites also leverage material hierarchy via fibrous reinforcement encapsulated within a polymer matrix, maximizing stiffness and strength. However, the layered architecture of laminated FRP composites makes them vulnerable to interlaminar delamination—debonding of fibers from the matrix—which significantly compromises structural integrity. Recently, we introduced a self-healing strategy via in situ heating, where soft yet tough thermoplastic inclusions achieve interlaminar fracture recovery via polymer chain re-entanglement, i.e., thermal remending. Here, in our latest embodiment, by automating in situ thermo-mechanical experiments, we achieve an order-of-magnitude enhancement in self-healing repeatability—reaching an unprecedented 1,000 cycles. Healing begins at 175% and slowly declines to 60% of the mode-I fracture resistance of a plain (nonhealing) composite, revealing unique chemo-physical mechanisms that govern this behavior. Both fiber-debris accumulation in the molten poly(ethylene-co-methacrylic acid) (EMAA) healing agent, and waning interfacial chemical reactions between the EMAA and epoxy matrix, contribute. A Weibull distribution capturing this complex fracture recovery predicts an asymptotic healing limit above 40%, suggesting sustained repair is possible. Translating these newfound thermal remending results into real-world context, a modest quarterly self-healing schedule could maintain interlaminar fracture repair of FRP composites for over 125 y—well beyond the typical design life of many modern structures including aircraft and wind turbines. Thus, this latest self-healing paradigm effectively eliminates delamination as a failure mode.

self-healing | fiber-composites | fracture

Composites combine different materials leveraging the unique advantages of each constituent, such as stiff/strong fibers providing load carrying capacity while an encapsulating matrix facilitates force transfer. Composite constructions are prevalent throughout nature, for instance, in the osseous tissue (i.e., bone) of vertebrates composed of hydroxyapatite-mineralized collagen (1), or cellulose microfibrils within the hemicellulose/lignin matrix of woody plants (2). In addition to providing mechanical integrity, biological structural composites also feature the ability to heal various types of injuries (e.g., fracture), and repeatably throughout the lifetime of the host organism (3–5). In this work, we sought to resolve the query: Is it possible for synthetic composites to achieve healing that is as robust and repeatable as natural counterparts? And if so, can we uncover the governing mechanisms and predict self-repair performance to guide engineers and designers in translating these materials into practical applications?

To that end, we demonstrate self-healing in FRP composites with unprecedented repeatability—sustaining 1,000 healing cycles, an order of magnitude beyond previous reports. To accelerate discovery, we developed an automated in situ electro-thermo-mechanical testing setup through integrated device and measurement systems. In contrast to the previously postulated "healing plateau" (6), our latest results reveal a progressive decline in fracture recovery, driven by synergistic chemical and physical aging mechanisms. Further analysis reveals that the experimental data closely follow a Weibull distribution. Extrapolation using this model predicts that recovery performance asymptotically approaches a nonzero lower bound (40%), thereby supporting the notion of sustained healing. Importantly, the acquired data forecast lifetime extensions ranging from 125 to 500 y under conservative healing and maintenance schedules—far exceeding the typical 40-y design life of modern composite infrastructure (e.g., aircraft). These findings provide

Significance

Delamination damage has long hindered the safety and lifetime of fiber-reinforced polymer composites. This failure mode not only undermines their lightweight mechanical advantage but also amplifies the cost and environmental impact of these modern structural materials, which are inherently challenging to repair/recycle. Here, we innovate self-healing by automating in situ thermal remending to achieve 1,000 delamination heal cycles, an order-of-magnitude greater than prior studies. The life extension unlocks new science where diminishing interfacial chemical reactions and fiber debris accumulation contribute to a gradual, asymptotic decline in fracture recovery that follows a Weibull distribution. Our findings show this self-healing strategy for interlaminar fracture is repeatable on a scale far exceeding typical composite design lifetimes, thus shedding delamination from structural concern.

Competing interest statement: The self-healing composite reported in this work has been issued a US patent (11,613,088B2) with J.F.P. listed as an inventor who is also the founding President and Chief Technology Officer of the company Structeryx, Inc. that has licensed this patent from North Carolina State University.

This article is a PNAS Direct Submission.

[1] To whom correspondence may be addressed. Email: jfpatric@ncsu.edu.

This article contains supporting information online at https://www.pnas.org/lookup/suppl/doi:10.1073/pnas.2523447123/-/DCSupplemental.

compelling evidence that our in situ thermal remending approach effectively eliminates the most critical failure mode in FRP composites—interlaminar delamination (7, 8).

Since their introduction in the 1930s, fiber-reinforced polymer (FRP) composites have been extensively adopted, primarily due to their superior material properties—namely, high specific stiffness and strength, as well as corrosion resistance—making them ideal for infrastructure across aerospace, naval, and wind-energy sectors, to name a few (9–12). However, the hierarchical architecture that imparts desirable structural attributes also makes FRP composites inherently vulnerable to complex damage (13–16). The associated damage modes range from fiber breakage to micron-scale matrix cracking between individual fibers to millimeter-scale delaminations that separate adjacent reinforcing plies (17, 18). Unlike biological materials, synthetic composites generally lack self-repair capabilities. Consequently, without timely manual intervention, damage accumulation leads to progressive deterioration of structural integrity and performance, which can ultimately result in catastrophic failure. Moreover, interlaminar delamination—often referred to as the most life-limiting damage mode (7, 8)—occurs subsurface, making it difficult to detect through visual inspection alone. While advanced nondestructive evaluation (NDE) techniques are available, their effectiveness varies and is often limited by the damage type and material heterogeneity (19, 20). Even if damage is located, current repair methods are labor intensive and usually involve removing larger portions than the affected region or complete component replacement, which is economically and environmentally costly (21, 22) given that fiber-composites are inherently difficult to recycle (23). To overcome these limitations, and drawing inspiration from nature's evolutionary elegance, diverse self-healing strategies have been developed over the past two decades to extend the useful lifetime of synthetic polymer and polymer-matrix composites (24, 25).

Mimicking osteonic canals in cortical bone and xylem/phloem in plants—which transport fluids for nutrient delivery and damage response—bioinspired microvascular strategies avail fracture-triggered release of reactive healing agents to autonomously fill and repair internal damage through in situ polymerization (26, 27). However, vascular-based and other "extrinsic" self-healing approaches that sequester an external agent [such as microcapsules (24, 28) or hollow fibers (29–31)] face limitations in repeatability due to the finite supply of healing agents, accumulation of polymerized "scar tissue" that impedes flow, and the inability to regenerate fluidic conduits, unlike biological systems (32, 33). "Intrinsic" self-healing strategies, by contrast, leverage reversible chemistry within a material to establish bond reformation after damage (34, 35). For example, in soft materials (e.g., gels) interfacial contact alone is often sufficient to facilitate intrinsic repair (36–40), but for structural polymers (e.g., thermosets), external energy input such as heat or light is normally required (41–44). Such intrinsic approaches alleviate scarring from foreign agents, promoting repeatability, and can operate on faster time scales than biological healing (minutes vs. days). A hybrid extrinsic/intrinsic self-healing approach requiring heat-activation and termed "thermal remending" has emerged for thermoset-matrix (e.g., epoxy) composites, whereby an external healing agent (e.g., thermoplastic) melts upon heating and solidifies upon cooling to provide fracture self-repair to the structural host (45–48). However, over the past 25 y, reliable and repeatable in situ self-healing in structural FRP composites has proven to be a formidable challenge due to experimental testing limitations and ex situ repair procedures (e.g., in an oven), along with difficulties finding fully compatible material systems (49).

Departing from status quo, in this work, we achieve sustained self-healing in FRP composites via a) thermal remending of a thermoplastic healing agent that is highly compatible with the native epoxy matrix, b) in situ heating leveraging embedded (electrically) resistive heaters, and c) integrated thermo-electro-mechanical testing protocol to automate the in situ experimentation (i.e., within the load frame). These innovations together enabled unprecedented repeatability in fracture recovery: 1,000 cycles—an order of magnitude greater than the current state-of-the-art (6).

Our healing agent, poly(ethylene-co-methacrylic acid) (EMAA) is a remendable copolymer, particularly well-suited for self-healing in thermoset epoxy-matrix composites owing to high fracture resistance (i.e., toughness) and strong interfacial bonding, sufficient melt flow for confined crack filling, and reformable ionic/hydrogen bonds at temperatures below the glass transition temperature (T_g) of the composite matrix, thereby preserving structural integrity during repair (50–53).

During thermal curing for epoxy cross-linking, covalent bonds form at the EMAA/epoxy interface enhancing the adhesion of the EMAA to the surrounding composite (Fig. 1*A*) (54). This strong bonding not only enhances fracture toughness, but it also directs damage to propagate cohesively through the thermoplastic domains resulting in EMAA on opposing fracture surfaces (Fig. 1*B*) (54, 55). A second condensation reaction initiated during curing produces small water bubbles which later vaporize during healing ($>100\,^{\circ}$C) to enact the well-documented EMAA pressure delivery mechanism–evidenced by a microporous network that also enhances crack tortuosity (i.e., fracture toughness) (51, 52). As the microporosity expands, it physically spreads EMAA and drives the molten polymer into multiscale cracks to enhance healing performance. Polymer chain entanglement [via hydrogen and ionic interactions (6, 53, 54)] rebonds fractured interfaces (Fig. 1*C*) for effective self-repair.

To our knowledge, only a few prior works (56, 57) and our own investigations (6, 53, 55, 58) have achieved in situ self-repair (e.g., via resistive heating), where others pursued ex situ healing (e.g., in an oven). Moreover, repeatability has remained a technical hurdle and has largely been limited to five (54, 59–61) or ten cycles (62), often with rapidly decaying performance. A recent study by our group investigated the evolution of these operant mechanisms over 100 in situ heal cycles (6), discovering EMAA microporosity cessation sooner in carbon- than glass-fiber composites owing to different surface chemical groups. Self-healing in each appeared to plateau—around 60% and 80% (relative to the virgin fracture resistance), respectively—by the centenary test cycle. Thus, it remained speculative that consistent self-healing would persist with subsequent cycling well-beyond this limit. However, the one hundred self-healing cycles—ten times any prior study at the time—was achieved by manual testing that took one month to complete for one sample and thus was not very practical to assess another order of magnitude (i.e., 1,000 cycles) in the same manner, which would have taken nearly a year to complete one experiment.

In this work, we developed an automated testing protocol by integrating electro-thermo-mechanical devices and measurements, enabling significantly accelerated data collection. This rapid testing approach allowed us to extend self-healing studies to 1,000 cycles, reducing the experimental timeline from twelve to just over one month. Beyond enabling high-throughput testing with exceptional repeatability, this innovation also provided

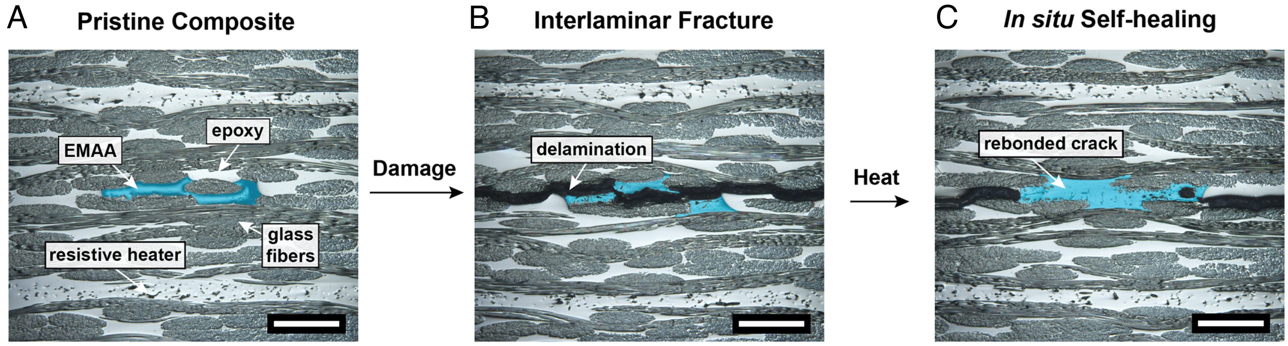

Fig. 1. Fiber-composite fracture and self-healing behavior. 3D-printed EMAA thermoplastic domains (blue color overlay) within the midplane of a glass-fiber epoxy-matrix composite laminate: (*A*) before damage, (*B*) post fracture, and (*C*) after self-healing via in situ thermal-remending (Scale bars, 0.5 mm).

newfound data critical for analyzing the long-term behavior of self-healing. As a result, we uncover previously inaccessible insights into the fundamental mechanisms governing self-repair, phenomena that had remained obscured due to prior limitations in testing methodology. Contrary to our prior healing plateau hypothesis (6), we reveal a steady decline in fracture recovery (from 175% to 60% of a plain glass-fiber composite) resulting from intertwined chemo-physical "aging" mechanisms. Extrapolations beyond the experiments—made by fitting the test data to a Weibull distribution—show asymptotic behavior that never falls below a minimum threshold of 40%, thus supporting the notion of sustained repair. Practically, we determine the maximum cycle count where healing remains above plain composite fracture resistance (i.e., 100%), resulting in lifetime extensions ranging from 125 to 500 y—for conservative healing/maintenance schedules—that now far exceed the typical design life of modern structures (≤40 y). Thus, we believe to have finally shown that this in situ thermal remending strategy can eliminate interlaminar delamination as the most critical failure mode in FRP composites (8).

1. Results and Discussion

1.1. Automated Fracture Testing. To reach 1,000 test cycles in a reasonable time (≈40 d), laboratory automation of mode-I fracture and thermal-based self-healing is developed. The damage-repair cycling is controlled via an in-house Python code that coordinates multiphysics (mechanical, thermal, electrical) equipment as detailed in Fig. 2*A*. An electromechanical test frame, with signal outputs read by a digital multimeter (DMM), applies displacement-controlled tensile loading to propagate a mode-I midplane delamination in a double cantilever beam (DCB) fracture specimen. During in situ healing, a DC power supply wired to resistive heaters embedded in the composite DCB provides electrical power for Joule heating, while an overhead infrared (IR) camera records the top surface temperature for on-the-fly calculations to preserve constant power input (i.e., heat flux) under changing conditions (i.e., electrical resistance). In-depth details regarding the test setup and hardware/software integration are provided in *SI Appendix*, section S1.

Fig. 2*B* provides a flowchart that illustrates the various steps/sequences to complete one test cycle, including fracture, resistive heating (which enables thermal remending for self-healing), and convective cooling; Fig. 2*C* shows fracture/heal cycle timing as well as the associated control signals. The test cycle begins with Step ①: the Python code enacting displacement-controlled loading via the electromechanical load frame. The DMM monitors the crosshead displacement to: ② detect when motion has begun, then taking displacement readings over the next 10 s to ③ determine via linear regression the precise displacement rate applied during loading. In Step ④, a relay then switches the DMM from monitoring displacement to force from the load cell in the test frame. In order to halt loading at a target incremental crack length (Δa) of 50 mm for each cycle, the first (i.e., virgin) fracture cycle is conducted manually, where the crack length is visually observed from below owing to the translucent sample. Then for subsequent "automated" testing, the instantaneous force vs. displacement is measured, and in Step ⑤ compared to the virgin fracture unload curve (*SI Appendix*, section S2) ensuring the crack is propagated to the same length in

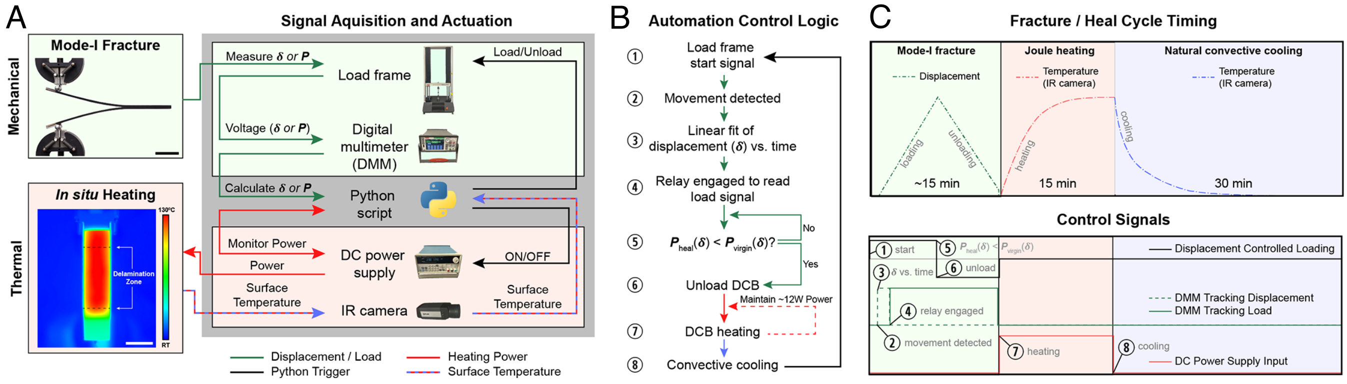

Fig. 2. Automated fracture/healing test protocol. (*A*) Flowchart of thermo-electro-mechanical signal acquisition and related actuation (Scale bar, 25 mm); (*B*) Automation control steps and logic for a single fracture/heal cycle; (*C*) (*Top*) Cycle timing schematic depicting mechanical loading and unloading, in situ resistive (i.e., Joule) heating, and natural convective cooling; (*Bottom*) Signal control diagram.

each cycle. Once the load-displacement response for the current cycle reaches the prescribed crack length (i.e., $\Delta a = 50$ mm), a signal is sent to the load frame to initiate Step ⑥: unloading the sample to zero crosshead displacement and closing the crack before healing commences. The 50 mm crack length and closure condition are selected in accordance to the ASTM standard (63). In Step ⑦, in situ heating is achieved by supplying ≈12 W to the embedded resistive heaters via the DC power supply. This raises the maximum surface temperature (as monitored via the IR camera) to a target value of 130 °C, which is below the glass-transition temperature of the composite (T_g ≈140 °C) to maintain structural integrity while healing. During Joule heating, the Python code continually records the voltage and current input to the heaters and automatically makes electrical current adjustments via the DC power supply to compensate for heater resistance fluctuations from thermal changes, thus maintaining a constant input power (i.e., heat flux). Heating is maintained for 15 min, followed by Step ⑧: 30 min of natural convective cooling to room temperature (RT) before the next fracture/heal cycle begins. One complete test cycle takes approximately 1 h, which is significantly faster than prior vascular healing cycles that take multiple days (64, 65). Thus, this latest automated in situ self-repair strategy can accomplish 1,000 heal cycles in just over one month of continuous testing.

1.2. Sustained In Situ Self-Healing. In our prior work, which achieved 100 nonautomated heal cycles, the restoration of fracture resistance (i.e., G_{IC}) appeared to plateau just above 80% of the virgin value (6). In that work, we hypothesized that self-healing would remain consistent beyond 100 cycles, but at the time, did not have the capabilities to generate sufficient evidence to validate such a claim. Thus, our aim with the present study is to leverage the latest automated fracture/healing protocol and extend the number of test cycles well beyond one hundred, in order to: i) evaluate the hypothesized perpetuity of in situ thermal remending, ii) determine any new mechanisms that affect fracture recovery under continued cycling, and iii) reveal whether self-healing on the order of modern composite structures' design life is possible. In short, we found that healing is sustained well beyond typical composite lifetimes, however with slowly waning recovery due to newly uncovered chemo-physical mechanisms discussed in subsequent sections.

Fig. 3*A* shows a double cantilever beam (DCB) specimen under tensile loading with a mode-I fracture (i.e., delamination) propagating along the EMAA-containing midplane. After the first fracture/heal cycle, the automated in situ testing protocol continues cycling the DCB to 1,000 cycles—for which the mechanical response (i.e., force–displacement) curves are provided in Fig. 3*B*. Initially, the force–displacement behavior increases linearly (as the composite arms bend elastically) until a midplane delamination propagates from the precrack, evidenced by a steady drop in force with crack growth. The nearly overlapping unload curves signify high reliability of the automated thermo-mechanical testing, more so than what is possible with manual testing. Consistent behavior is observed across cycles, with a gradual reduction in healed fracture resistance depicted by the shrinking area contained within the force–displacement curves. Mode-I fracture performance for each cycle is quantified by the critical strain energy release rate (G_{IC})—a measure of the energy (ΔU) required to propagate the crack—and compared in Fig. 3*C* to prior state-of-the-art EMAA-based self-healing composite technologies from: 2016 with 5 heal cycles (54) and 2022 with 100 heal cycles (6). It should be emphasized that plain composite control samples (containing no EMAA) exhibit negligible fracture recovery after in situ heating at the same temperature (i.e., 130 °C), which is below the T_g of the cross-linked epoxy limiting matrix molecular mobility for recovery. The virgin fracture resistance of the present EMAA-modified composite ($G_{\mathrm{IC}} = 1{,}333$ J/m^2) is roughly threefold higher than a plain composite (≈430 J/m^2). Maximum healing (i.e., G_{IC} recovery) occurs at test cycle 7, due in large part to molten EMAA spreading, and is above 230% of the nonhealing plain composite control. The fracture recovery then slowly declines, reaching 180% by heal cycle 100 and 60% by cycle 1,000. The higher G_{IC} healing response reported by Snyder et al. (6)—up to 100 cycles—using the same woven glass-fiber reinforcement and 3D-printed EMAA material/pattern/process, is attributed to a different epoxy matrix, which highlights the importance of chemical interactions between the healing agent and host matrix (53). Despite lower G_{IC} values for the first hundred cycles, the latest self-healing data spanning 1,000 cycles, shows a slow but diminishing decline in fracture recovery. In fact, for the last hundred cycles, the average healed fracture resistance only decreases at a rate of ≈0.1%/cycle, indicating that recovery may eventually plateau as originally hypothesized in 2022, but at a much greater cycle count. Better understanding of the governing physical and chemical mechanisms responsible for the observed healing behavior is necessary to further support such a perpetuity prediction.

1.3. Physical Healing Mechanisms. To investigate the physical mechanisms (at different size-scales) that may impact healing performance over extended cycling, both optical and electron microscopy are performed. Optical images shown in Fig. 3*D*, *Top row* reveal a crack plane with fairly uniformly distributed matrix/fiber/EMAA domains over the first 10 heal cycles. However, as the 100th cycle is reached, there is noticeably more glass-fiber topology on the fracture surface, which becomes even more apparent by heal cycle 1,000. We believe that this increased fiber prominence is the result of: i) EMAA strongly adhering to the epoxy matrix that is debonded from the underlying reinforcement during fracture and ii) continual fiber-bridging/rupture that increases fiber debris accumulation in the EMAA healing agent with further cycling. In early cycles, fiber debris appears to concentrate along the continuous tows indicated by the white striations in the crack plane, while by cycle one thousand, a pervasive fibrous zone is observed nearly spanning the full sample width and ≈25 mm along the length from the terminal crack front. We believe the fiber debris accumulation is higher in this region due to smaller crack separations and thus higher propensity for crushing any protruding fibers during unloading; though discrete fibrous regions up to the point of crack initiation are also observed, emphasizing the widespread nature of this newly discovered mechanism. A prominent color change (i.e., browning) is also visible by the final cycle, on both the fracture and outer surfaces of the composite, likely owing to oxidation of the amine-containing thermoset epoxy matrix that is accelerated by repeated heating at ten degrees below the glass transition (T_g ≈ 140 °C; onset of T_g ≈ 120 °C). However, we do not expect this oxidation in trace amounts to interfere with key chemical reactions between the epoxy matrix and EMAA healing agent which are investigated via spectroscopy in the next section.

A closer inspection of the composite fracture topology is conducted via scanning electron microscopy (SEM) with respective images shown in Fig. 3*D*, *Bottom row*. After the virgin fracture, ductile tearing of the EMAA is evident along

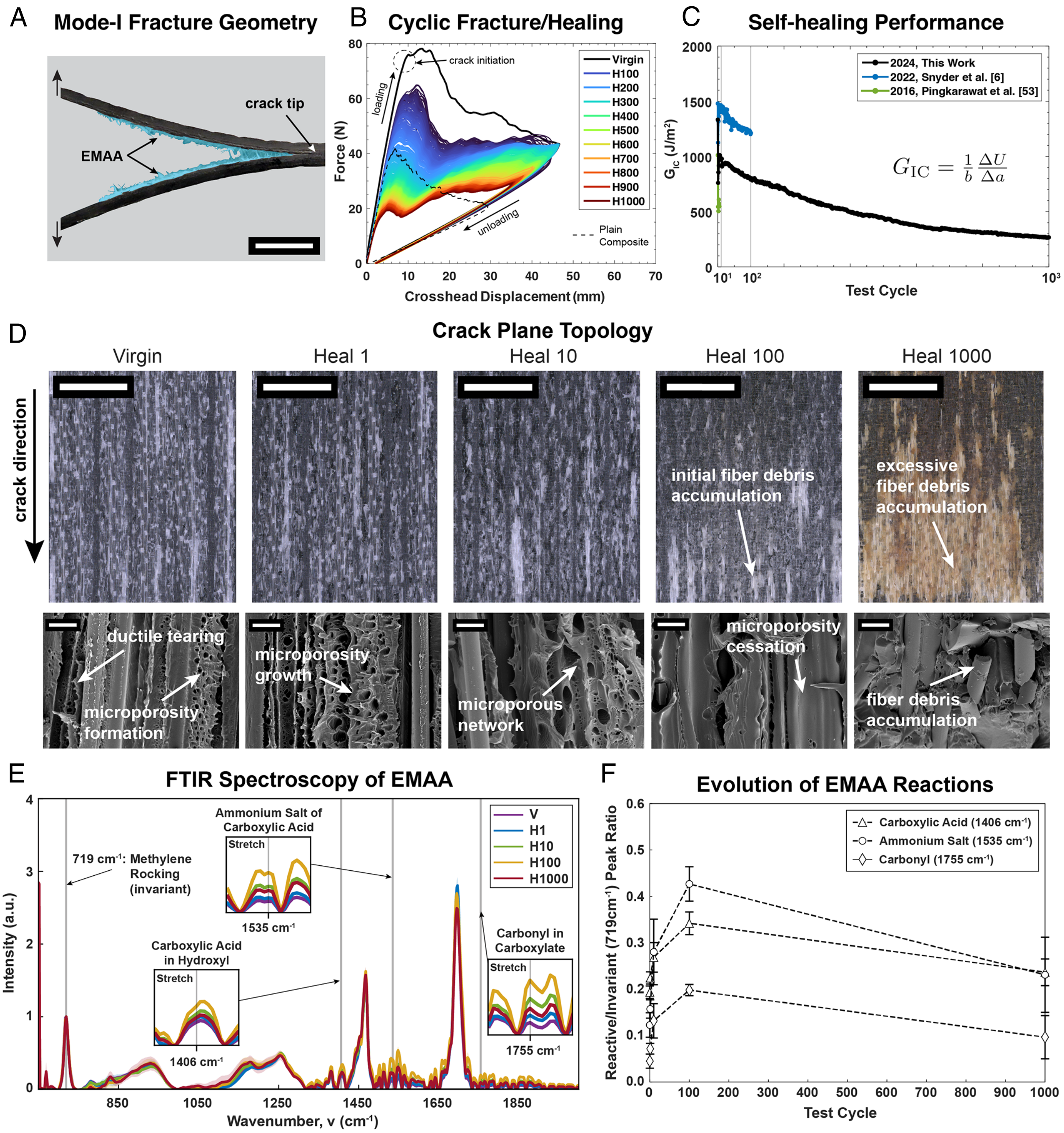

Fig. 3. Sustained in situ self-healing. (*A*) Mode-I interlaminar fracture of a glass-fiber composite double cantilever beam (DCB) showing EMAA fibrillation (55) (Scale bar, 10 mm); (*B*) Overlaid force vs. displacement curves for virgin and 1,000 heal cycles along with a plain, nonhealing composite response (dashed line); (*C*) Self-healing performance comparing the cyclic fracture resistance (i.e., G_{IC}) of the present study to prior state-of-the-art EMAA-based technologies (6, 54); (*D*) Optical and scanning electron micrographs revealing midplane fracture topology after the virgin and heal cycles 1, 10, 100, and 1,000 [Scale bars, 10 mm (*Top*) and 10 µm (*Bottom*)]; (*E*) Fourier transform infrared (FTIR) spectra of key EMAA chemical species after the virgin and select heal cycles where the line thickness represents one SD from the mean ($n \geq 5$); (*F*) Evolution of FTIR peaks from key reactive groups: carboxylic acid hydroxyl stretch (1,406 cm^{-1}), carboxylic acid ammonium salt stretch (1,535 cm^{-1}), and carbonyl stretch (1,755 cm^{-1}) that are normalized to the peak for an invariant species: methylene rocking (719 cm^{-1}); error bars represent one SD from the mean ($n \geq 5$).

with microporosity formation, which stems from vaporizing entrapped water (by healing above 100 °C) that is first formed via the well-documented condensation reaction during composite curing (51, 52, 54). The microporous network, which contributes to toughening via crack tortuosity, continues to expand with further cycling through heal 10, but then slowly wanes and is nearly collapsed by heal 100, where the EMAA domains exhibit a smooth surface. The development and cessation of microporosity over the first 100 cycles aligns well with our findings in prior work (6). However, the latest finding of fiber debris accumulation at higher cycle counts, which is also observed in the SEM images, noticeably obstructs EMAA rebonding sites and likely contributes to the slow decline in fracture recovery. Hence, akin to vascular self-healing systems where healed polymer accumulation (i.e., scarring) limits repeatability (64, 65), this latest thermal remending approach is also subject to inevitable decline in self-repair, but with several orders of magnitude greater repeatability. In other words, where extrinsic vascular-based scarring from polymerized healing agent quickly diminishes repair performance due to obstructed channel orifices that inhibit further liquid healing agent delivery, intrinsic thermal remending via a finite volume of EMAA maintains self-repair efficacy longer even in the presence of scarring from host material debris accumulation. In addition to this physical phenomenon, we hypothesize that molecular interactions also affect healing perseverance.

1.4. Chemical Healing Mechanisms. The unique molecular interactions for EMAA-epoxy systems are vital to: i) obtain strong bonding between the thermoplastic healing agent and thermoset composite host, ii) activate the pressure delivery (i.e., microporosity) mechanism to help spread EMAA, and iii) to enable repeated self-repair of fracture resistance via polymer chain entanglement (6, 53). During the fiber-composite cure (up to 177 °C), two competing reactions dominate involving carboxylic acid (from EMAA) and either epoxide (from the matrix) or hydroxyl groups (from the matrix and reinforcement). The carboxylic acid/epoxide reaction is largely responsible for the strong covalent bonding at the EMAA/epoxy interface, promoting cohesive fracture of EMAA, which is key to repeated healing. While the carboxylic acid/hydroxyl condensation reaction—occurring later during curing as catalyzed by tertiary amines—contributes to the EMAA/epoxy interfacial bond, it also produces small liquid water domains within the EMAA that vaporize during healing forming the microporous network (Fig. 3*D*). Such reactions were examined in earlier work (6) and shown to wane with continued cycling resulting in eventual cessation of microporosity, but retention of healing that is primarily due to EMAA hydrogen bonding. However, the evolution of molecular interactions beyond 100 cycles remained unexplored due to aforementioned testing limitations.

Ergo, here we probed these key chemical reactions using Fourier-transform infrared (FTIR) spectroscopy in attenuated total reflectance (ATR) mode on the fracture surface of composite samples in the virgin and healed states (cycles 1, 10, 100, 1,000). The absorbance spectra related to three key chemical species that participate in the covalent/ionic bonding of EMAA to the host composite (6, 51, 52)—carboxylic acid hydroxyl stretch (1,406 cm^{-1}), carboxylic acid ammonium salt stretch (1,535 cm^{-1}), carbonyl stretch (1,755 cm^{-1})—are normalized to the invariant methylene rocking peak (719 cm^{-1}) and plotted in Fig. 3*E*. The reactive to invariant peak ratios are quantified in Fig. 3*F* and show that these chemical species increase over the first 100 cycles. This coincides with EMAA microporosity development and spreading, which both give rise to increased fracture resistance via crack tortuosity and greater coverage of the tough thermoplastic, followed by waning and eventual cessation of microporosity whereby covalent chemical interactions persist and mitigate decline in fracture recovery. Over the next 900 cycles (i.e., previously unexplored healing regime) the chemical species/reactions decrease as the fracture performance also slowly declines (Fig. 3*C*). However, some level of self-healing is maintained due to sustained hydrogen bonding (i.e., polymer chain entanglement) despite the reduced proportion of bonding sites that are impeded by glass-fiber debris. These latest findings show that self-healing via thermal remending is an intricate interplay of both chemical and physical mechanisms, where waning covalent interactions and accumulation of fiber microdebris contribute to a slow decline in fracture recovery.

1.5. Self-Healing Lifetime Prediction. While experiments were terminated at 1,000 cycles, strong evidence of steadying fracture recovery becomes apparent (i.e., G_{IC} only decreases at an average rate of ≈0.1%/cycle over the last 100 cycles). Given the high repeatability of the fracture/healing behavior, analytical models can extrapolate well beyond what has been demonstrated in the lab. Given its precedence in modeling fracture damage in composites (70–73), we find that the probability density function for a Weibull distribution fits the data particularly well, as shown in Fig. 4*A*. The model is fit to the experimental self-healing data over the declining portion (i.e., heal cycle 10 through 1,000) and normalized to the fracture energy of the first heal cycle (≈760 J/m^2). The Weibull shape factor (k) is ≈1.01, which is appropriate for predicting the failure of systems that slowly degrade over time (74). For our self-healing system, the Weibull fit predicts an asymptotic lower limit of fracture recovery around 44% (compared to a plain composite) and remains above this value by the millionth heal cycle, suggesting that self-healing can be "perpetual," albeit at nearly half the fracture resistance of a plain composite.

Self-healing performance for the EMAA-enhanced fiber composite first dips below the value of a plain composite on test cycle 505, which essentially defines the point at which component replacement would be necessary to meet original

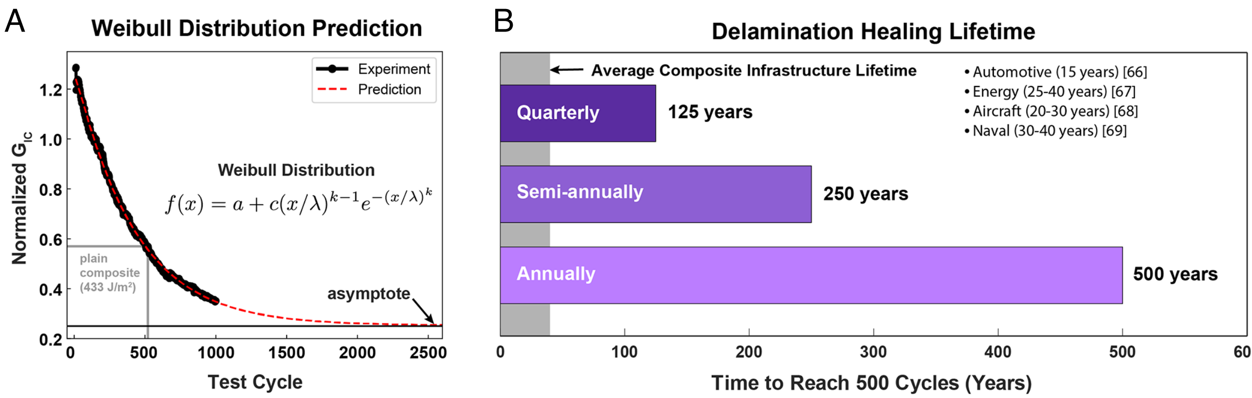

Fig. 4. Lifetime prediction for delamination healing. (*A*) Weibull distribution overlaid with experimental test data for heal cycles 10 to 1,000 with fracture resistance (i.e., G_{IC}) normalized to the value in the first heal cycle; (*B*) Estimated self-healing lifetime for interlaminar delamination recovery based upon the maximum heal cycle (505) before reaching plain composite fracture toughness for quarterly, semiannual, and annual repair schedules with average composite design life listed for various industries (i.e., automotive, energy, aircraft, naval) (66–69).

design specifications. To put this newfound self-healing capacity into real-world context of modern composite structures (e.g., aircraft), we examined typical maintenance schedules. Commercial aircraft undergo routine inspection/maintenance that may include nondestructive evaluation (e.g., ultrasound scanning) according to A, B, C, and D schedules (75, 76). A-checks are performed every 400 to 600 flight hours (≈200 to 300 flights) and encompass overnight inspections/servicing of internal systems, emergency equipment, and other specific components (e.g., landing gear, primary structure). B-checks take place every 6 to 8 mo and delve deeper into the aircraft's systems and structure, requiring around 160 to 180 human-hours to complete. C-checks are more comprehensive evaluations including in-depth structural inspections and occur every 20 to 24 mo, requiring grounding for 1 to 4 wk and up to 6,000 h of crew labor. D-checks take place every 6 to 12 y for heavy-maintenance that includes a nearly complete overhaul with detailed inspection and repair of the structural elements including airframe, wings, tail, etc.

Given our self-healing system targets interlaminar fracture recovery in structural elements, we consider conservative repair schedules of 3, 6, and 12 mo (i.e., quarterly, semiannually, and annually) to predict the delamination healing lifetime this technology could provide being applied either in situ (e.g., on the tarmac) or ex situ (e.g., in a hangar)—acknowledging that other failures may still occur. Such projections plotted in Fig. 4*B* estimate the fracture repair lifetime of our self-healing composites range from 125 to 500 y, which greatly exceeds the design life of modern aircraft (20 to 30 y) and other real-world composite structures in the automotive (66), energy (67), aerospace (68), and naval (69) industries. From an interstellar perspective, a composite spacecraft traveling at the same speed of the international space station (≈28,000 km/h) would reach Pluto and return to Earth in roughly 60 y, and have better odds of surviving high-speed collisions with foreign objects (e.g., micrometeoroids) being outfitted with such self-healing technology. While in operando (e.g., in-flight) self-healing demonstrators under actual load are still needed to validate such space platforms, we believe that our reliable and repeatable in situ thermal remending strategy can eliminate delamination as a failure concern across these and countless other applications of structural FRP composites.

2. Conclusion

In this work, we overcome interlaminar delamination that has long plagued composite structures, degrading performance and limiting service life (8). We authenticate the ability of an aerospace-grade composite to heal mode-I fracture damage, in situ, and below the epoxy matrix glass transition temperature for 1,000 consecutive cycles—approaching the reliability of self-repair observed in natural materials, albeit through a synthetic pathway. An autonomous fracture/healing protocol is established to experimentally realize the feat over one month of continuous testing, which also highlights the amenability of this thermal remending technique to industrial automation. We want to highlight that while this testing protocol is autonomous, material-level autonomy (77) in a real-world structure would require integrated damage-sensing to automatically trigger heating and enact self-repair mechanisms before reaching critical flaw sizes (49). Moreover, we only consider delamination recovery after mode-I tensile loading owing to this being the lowest energy fracture pathway but expect self-healing of interlaminar fracture to be agnostic to the mode of generation/propagation (i.e., I, II, or III). However, other possible failures such as matrix-cracking and fiber-breakage, along with mode-mixity that can arise from complex loading (e.g., impact) need to be further explored. Some promising recent work has shown that EMAA-patterned interlayers (at low volume fractions) preserve the thermo-mechanical properties of laminated composites (6, 55) and steer damage during shear-dominated flexure toward healable delamination (58).

Here, our investigation of the governing chemo-physical self-healing mechanisms after mode-I fracture reveals fiber debris buildup in the crack plane and the waning of key healing reactions—between the EMAA healing agent and epoxy matrix composite—producing a slow and steady decline in fracture recovery after achieving a maximum of 230% relative to a plain composite baseline. The consistency in self-repair enables analytical models to extrapolate healing behavior well beyond experiments, where the predicted asymptotic delamination recovery is nearly one half the pristine fracture resistance value of a conventional composite, but theoretically in perpetuity. These findings also show that the ability to remain above plain composite fracture resistance via a conservative quarterly self-healing schedule exceeds three times the design life of real-world composite structures (> 125 y), and effectively ousts delamination as a critical failure mode in fiber-reinforced polymer composites.

3. Materials and Methods

3.1. 3D-Printing EMAA. EMAA filament is first extruded to a diameter of ≈2.5 mm from as-purchased pellets (Nucrel™ 2940, DuPont, Inc.) using a single screw extruder (Noztek Pro) with a barrel temperature of 110 °C and a 3 mm diameter circular die. Extruded filament is cooled on a rotating steel take-up cylinder to room temperature (RT ≈ 24 °C) by forced convection from a nearby fan.

The EMAA filament is then 3D-printed onto 8-harness (8H) satin woven E-glass reinforcement (Style 7781, Hexcel, Inc.) using a fused deposition modeling (FDM) printer (TAZ Pro, Lulzbot, Inc.) equipped with a 500 μm diameter nozzle heated to 190 °C with a build platform temperature of 65 °C. EMAA is printed along a continuous serpentine path with traces ≈350 ± 50 μm thick and ≈500 ± 50 μm wide that are spaced 2.2 mm apart center to center and extend 80 mm from the interior edge of the precrack film to meet the prescribed as-printed areal coverage of 24%.

3.2. Resistive Heater Preparation. Two layers of proprietary resistive heaters (≈100 μm thick) consisting of a nonwoven carbon/glass textile are cut to 140 mm wide by 305 mm long. A 20 mm wide conductive silver coating is applied to the outer side of each layer, full width at the two edges along the length. The coating is dried for 30 min at room temperature (RT) before adhering 20 mm wide strips of conductive copper tape along the painted regions, serving as a busbar for external electrical connections.

3.3. Preform Construction and Melt Consolidation. Preforms comprise three EMAA interlayers located below/at/above the midplane and two resistive heaters (H) spaced symmetrically above/below with a stacking sequence of $[90/0]_2$/90/H/0/90-EMAA-0-EMAA-90-EMAA-0/90/H/0/$[90/0]_2$. Despite controlled fracture propagation along the midplane, EMAA interlayers are required in the adjacent layers to prevent out-of-plane delaminations therein with repeated cycling. A 50 μm thick fluoropolymer film (50 mm wide by 305 mm long) is placed at the midplane and aligned with the start of the 3D-printed EMAA patterns to serve as a precrack for fracture experiments.

Melt consolidation of EMAA is achieved by placing the layered preform between two aluminum plates (405 × 405 × 6.35 mm, length × width × thickness) which are weighted to provide 1 kPa of applied pressure relative to the preform surface area. The weighted assembly is placed in a convection oven (OF-22, Cole-Parmer, Inc.) and heated from RT to 110 °C over 15 min where the temperature is held for 75 min before cooling to 60 °C over 90 min. The preform is then removed from the oven and cooled to RT.

3.4. Vacuum-Assisted Resin Transfer Molding (VARTM). A proprietary epoxy-based resin and amine-based hardener system are mixed at stoichiometry and degassed for 2 h at RT under 12 Torr (abs) vacuum in a drying oven (ADP 300C, Yamato, Inc.). Vacuum assisted resin transfer molding (VARTM) is performed at 2 Torr (abs) to infuse the preform assembly with the liquid matrix until complete fabric wetting. Vacuum is then decreased to 380 Torr (abs) and held for 24 h at RT until matrix solidification. Next, the vacuum is removed and the laminates are cured for 2 h at 121 °C followed by 3 h at 177 °C to yield a final glass-transition temperature (T_g) of ≈141 °C as measured by dynamic mechanical analysis (DMA).

3.5. Mode-I Fracture Characterization.

3.5.1. Fracture specimen fabrication. Fracture specimens are sectioned to 25 mm wide by 140 mm long with a diamond-blade wet saw (Sowers 41-AR). A 0.65 mm diameter hole is drilled ≈4 mm into each of the heater busbars on both the front and back ends of the specimens (four holes total), where copper wires (0.64 mm diameter) are inserted and potted with a commodity two-part epoxy (The Gorilla Glue Company, Inc.). Steel piano hinges are bonded to the top/bottom faces of the composite along the front (i.e., precrack) end of the sample with a structural adhesive (DP460NS, 3M, Inc.) that is cured for 4 h at 49 °C. A straight line perpendicular to the crack direction is marked at 50 mm from the interior edge of the precrack film to demarcate the total distance of crack propagation. The top face of each specimen is painted flat black for infrared (IR) imaging during in situ healing.

3.5.2. Mode-I fracture testing and in situ thermal remending. Double-cantilever beam (DCB) mode-I fracture tests are performed according to ASTM D5528 on a 5 kN electromechanical load frame (Alliance RT/5, MTS, Inc.) with a 500 N load cell. Displacement controlled loading at a rate of 5 mm/min is enacted to propagate a 50 mm long midplane delamination from the precrack film. A 4K resolution webcam (Logitech BRIO), equipped with a custom macrolens (LM12JC5M2, Kowa Optical Products Co., Ltd.), is used to monitor the crack from the bottom surface of the translucent glass-fiber composites and the loading is stopped once the crack reaches the marked termination line. The sample is then unloaded at the same rate to zero crosshead displacement.

After unloading, in situ self-healing is accomplished by activation of a DC power supply (PWS4602, Tektronix, Inc.) providing ≈12 W of electrical power to the embedded resistive heaters. Joule heating progresses for 15 min to a target maximum surface temperature of 130 °C as monitored by an overhead IR camera (A600, Teledyne FLIR, Inc.), which is below the T_g of the composite (≈141 °C). The power is then deactivated and the sample cools via natural convection to RT over a ≈30 min period before the next fracture/heal cycle commences. Note, the first (i.e., virgin) test cycle is performed manually to: i) generate the unload curve after 50 mm of crack propagation which is used as a loading termination condition (i.e., trigger the switch from loading to unloading) for subsequent automated fracture tests, and ii) determine the exact power input to the embedded heaters that is required to reach the target healing temperature (130 °C), which varies slightly (±0.5 W) between samples. After the virgin cycle is complete, automated testing is enacted via load frame signal acquisition by a digital multimeter (DMM7510, Keithley Instruments) and following the test protocol detailed in the main text.

3.5.3. Fracture quantification. Fracture resistance is quantified via calculation of the mode-I critical strain energy release rate (G_{IC}) for each cycle, which is a measure of the energy required to propagate a crack normalized by the planar area of the newly fractured interface (i.e., sample width × crack length). In this study, the area method (78) is chosen to calculate a single G_{IC} value for each fracture cycle according to:

$$G_{IC} = \frac{1}{b}\frac{\Delta U}{\Delta a}, \qquad [1]$$

where b is the sample width, Δa is the linear crack propagation distance, and ΔU is the energy required to create the fractured surfaces, which is defined by the area enclosed within the load-displacement curve (loading and unloading):

$$\Delta U = \int_0^{\delta} P\, d\delta \bigg|_{\Delta a}, \qquad [2]$$

where P, is the resulting force from the applied displacement, δ.

3.6. Topological Characterization of Fracture Surfaces. Optical and scanning electron microscopy (SEM) are used to investigate the surface morphology of fractured/healed interfaces. Optical images are acquired with a digital light microscope (AXIO Zoom V.16, Zeiss, Inc.) equipped with an LED ring light or coaxial polarizer. For SEM, samples are first sputtered with gold/palladium to a target coating thickness of ≈35 nm before imaging with a variable pressure scanning electron microscope (S3900N, Hitachi, Ltd.) at a 5 kV accelerating voltage.

3.7. Chemical Characterization of Fracture Surfaces. Fourier-transform infrared (FTIR) spectroscopy (HYPERION 1,000, Bruker, Inc.) is performed on fractured/healed interfaces in attenuated total reflectance (ATR) mode, utilizing a 70 μm germanium crystal probe and 15x objective. Thirty-two scans are collected at each site from the 4,000 to 650 cm^{-1} wavenumber range.

3.8. Analytical Predictions. A probability density function of the Weibull distribution:

$$f(x) = a + c(x/\lambda)^{k-1}e^{-(x/\lambda)^k} \qquad [3]$$

is fit to the fracture energy (i.e., G_{IC}) results from heal cycle 10 to heal cycle 1,000 to model and predict the self-healing performance beyond what is experimentally evaluated. All values are normalized to the G_{IC} of the first heal cycle (761 $\mathrm{J/m^2}$). Here, the curve fit gives $a = 0.2526$, $c = 1.052$, a shape parameter of $k = 1.010$, and a scale parameter of $\lambda = 38.09$.

Data, Materials, and Software Availability. Relevant data in CSV format have been made publicly available on Zenodo (DOI: 10.5281/zenodo.17845142) (79).

ACKNOWLEDGMENTS. We acknowledge the financial support from the Strategic Environmental Research and Development Program through grant No. W912HQ21C0044 awarded to J.F.P. This material is based upon work supported by the National Science Foundation (NSF) Graduate Research Fellowship Program for J.S.T. under Grant No. DGE-2137100. The work was performed in part at the Analytical Instrumentation Facility at North Carolina State University, which is supported by the State of North Carolina and the NSF (grant ECCS-2025064). The authors extend their gratitude to Dr. Carrie Donley at the Chapel Hill Analytical and Nanofabrication Laboratory for assistance with spectroscopy and Cindy Ashforth at the Federal Aviation Administration for insight into commercial aircraft maintenance.

Author affiliations: [a]Department of Mechanical and Aerospace Engineering, North Carolina State University, Raleigh, NC 27695; [b]Department of Civil, Construction, and Environmental Engineering, North Carolina State University, Raleigh, NC 27695; and [c]Department of Civil and Environmental Engineering, University of Houston, Houston, TX 77204

Author contributions: J.F.P. designed the research and acquired funding; J.S.T. and Z.J.P. performed the experiments; and J.S.T., Z.J.P., K.B.N., and J.F.P. analyzed data and wrote the paper.

1. A. A. Poundarik *et al.*, Dilatational band formation in bone. *Proc. Natl. Acad. Sci. U.S.A.* **109**, 19178–19183 (2012).
2. A. N. Fernandes *et al.*, Nanostructure of cellulose microfibrils in spruce wood. *Proc. Natl. Acad. Sci. U.S.A.* **108**, E1195–E1203 (2011).
3. P. Fratzl, R. Weinkamer, Nature's hierarchical materials. *Prog. Mater. Sci.* **52**, 1263–1334 (2007).
4. U. G. K. Wegst, H. Bai, E. Saiz, A. P. Tomsia, R. O. Ritchie, Bioinspired structural materials. *Nat. Mater.* **14**, 23–36 (2015).
5. A. F. van Tol *et al.*, The mechanoresponse of bone is closely related to the osteocyte lacunocanalicular network architecture. *Proc. Natl. Acad. Sci. U.S.A.* **117**, 32251–32259 (2020).

6. A. D. Snyder *et al*., Prolonged in situ self-healing in structural composites via thermo-reversible entanglement. *Nat. Commun.* **13**, 1–12 (2022).
7. J. K. Kim, M. L. Sham, Impact and delamination failure of woven-fabric composites. *Compos. Sci. Technol.* **60**, 745–761 (2000).
8. M. R. Wisnom, The role of delamination in failure of fibre-reinforced composites. *Philos. Trans. R. Soc. A Math. Phys. Eng. Sci.* **370**, 1850–1870 (2012).
9. N. R. Council, *High-Performance Structural Fibers for Advanced Polymer Matrix Composites* (The National Academies Press, Washington, DC, 2005).
10. B. De, M. Bera, D. Bhattacharjee, B. C. Ray, S. Mukherjee, A comprehensive review on fiber-reinforced polymer composites: Raw materials to applications, recycling, and waste management. *Prog. Mater. Sci.* **146**, 101326 (2024).
11. M. Puttegowda, S. Rangappa, S. Siengchin, *Fiber-Reinforced Polymer Composites: Materials and Manufacturing* (Woodhead Publishing, 2025).
12. C. T. Herakovich, Mechanics of composites: A historical review. *Mech. Res. Commun.* **41**, 1–20 (2012).
13. D. Hull, Matrix-dominated properties of polymer matrix composite materials. *Mater. Sci. Eng. A* **184**, 173–183 (1994).
14. G. A. Bibo, P. J. Hogg, The role of reinforcement architecture on impact damage mechanisms and post-impact compression behaviour. *J. Mater. Sci.* **31**, 1115–1137 (1996).
15. F. Lamon, L. Maragoni, P. A. Carraro, M. Quaresimin, Fatigue damage evolution in woven composites with different architectures. *Int. J. Fatigue* **167**, 107365 (2023).
16. R. Talreja, Assessment of the fundamentals of failure theories for composite materials. *Compos. Sci. Technol.* **105**, 190–201 (2014).
17. W. J. Cantwell, J. Morton, The significance of damage and defects and their detection in composite materials: A review. *J. Strain Anal. Eng. Des.* **27**, 29–42 (1992).
18. V. Giurgiutiu, "Chapter 5 - Damage and failure of aerospace composites" in *Structural Health Monitoring of Aerospace Composites* (Academic Press, 2016), pp. 125–175.
19. B. Wang, S. Zhong, T. L. Lee, K. S. Fancey, J. Mi, Non-destructive testing and evaluation of composite materials/structures: A state-of-the-art review. *Adv. Mech. Eng.* **12**, 1–28 (2020).
20. M. M. Azad *et al*., Failure modes and non-destructive testing techniques for fiber-reinforced polymer composites. *J. Mater. Res. Technol.* **33**, 9519–9537 (2024).
21. K. B. Katnam, L. F. M. Da Silva, T. M. Young, Bonded repair of composite aircraft structures: A review of scientific challenges and opportunities. *Prog. Aerosp. Sci.* **61**, 26–42 (2013).
22. R. B. Heslehurst, *Engineered Repairs of Composite Structures* (CRC Press / Taylor & Francis, Boca Raton, ed. 1, 2019).
23. R. S. Stein, Polymer recycling: Opportunities and limitations. *Proc. Natl. Acad. Sci. U.S.A.* **89**, 835–838 (1992).
24. S. R. White *et al*., Autonomic healing of polymer composites. *Nature* **409**, 794–797 (2001).
25. B. J. Blaiszik *et al*., Self-healing polymers and composites. *Annu. Rev. Mater. Res.* **40**, 179–211 (2010).
26. C. E. Diesendruck, N. R. Sottos, J. S. Moore, S. R. White, Biomimetic self-healing. *Angew. Chem. Int. Ed.* **54**, 10428–10447 (2015).
27. J. F. Patrick, M. J. Robb, N. R. Sottos, J. S. Moore, S. R. White, Polymers with autonomous life-cycle control. *Nature* **540**, 363–370 (2016).
28. E. N. Brown, S. R. White, N. R. Sottos, Microcapsule induced toughening in a self-healing polymer composite. *J. Mater. Sci.* **39**, 1703–1710 (2004).
29. J. W. C. Pang, I. P. Bond, A hollow fibre reinforced polymer composite encompassing self-healing and enhanced damage visibility. *Compos. Sci. Technol.* **65**, 1791–1799 (2005).
30. R. S. Trask, G. J. Williams, I. P. Bond, Bioinspired self-healing of advanced composite structures using hollow glass fibres. *J. R. Soc. Interface* **4**, 363–371 (2007).
31. A. Kousourakis, A. P. Mouritz, The effect of self-healing hollow fibres on the mechanical properties of polymer composites. *Smart Mater. Struct.* **19**, 1–9 (2010).
32. I. P. Qamar, N. R. Sottos, R. S. Trask, Grand challenges in the design and manufacture of vascular self-healing. *Multifunct. Mater.* **3**, 013001 (2020).
33. V. Chano, R. López, P. Pita, C. Collada, Á. Soto, Proliferation of axial parenchymatic xylem cells is a key step in wound closure of girdled stems in *Pinus canariensis*. *BMC Plant Biol.* **15**, 64 (2015).
34. A. Cohades, C. Branfoot, S. Rae, I. Bond, V. Michaud, Progress in self-healing fiber-reinforced polymer composites. *Adv. Mater. Interfaces* **5**, 1–20 (2018).
35. S. J. Garcia, Effect of polymer architecture on the intrinsic self-healing character of polymers. *Eur. Polym. J.* **53**, 118–125 (2014).
36. P. Cordier, F. Tournilhac, C. Soulié-Ziakovic, L. Leibler, Self-healing and thermoreversible rubber from supramolecular assembly. *Nature* **451**, 977–980 (2008).
37. K. Imato *et al*., Self-healing of chemical gels cross-linked by diarylbibenzofuranone-based trigger-free dynamic covalent bonds at room temperature. *Angew. Chem. Int. Ed.* **51**, 1138–1142 (2012).
38. Z. Wei *et al*., Self-healing gels based on constitutional dynamic chemistry and their potential applications. *Chem. Soc. Rev.* **43**, 8114–8131 (2014).
39. D. L. Taylor, M in het Panhuis, Self-healing hydrogels. *Adv. Mater.* **28**, 9060–9093 (2016).
40. A. Phadke *et al*., Rapid self-healing hydrogels. *Proc. Natl. Acad. Sci. U.S.A.* **109**, 4383–4388 (2012).
41. X. Chen *et al*., A thermally re-mendable cross-linked polymeric material. *Science* **295**, 1698–1702 (2002).
42. J. S. Park, H. S. Kim, H. Thomas Hahn, Healing behavior of a matrix crack on a carbon fiber/mendomer composite. *Compos. Sci. Technol.* **69**, 1082–1087 (2009).
43. D. Montarnal, M. Capelot, F. Tournilhac, L. Leibler, Silica-like malleable materials from permanent organic networks. *Science* **334**, 965–968 (2011).
44. H. Sharma *et al*., Self-healable fiber-reinforced vitrimer composites: Overview and future prospects. *RSC Adv.* **12**, 32569–32582 (2022).
45. S. A. Hayes, W. Zhang, M. Branthwaite, F. R. Jones, Self-healing of damage in fibre-reinforced polymer-matrix composites. *J. R. Soc. Interface* **4**, 381–387 (2007).
46. A. R. Jones, C. A. Watkins, S. R. White, N. R. Sottos, Self-healing thermoplastic-toughened epoxy. *Polymer* **74**, 254–261 (2015).
47. V. M. A. Cohades, Thermal mending in E-glass reinforced poly(ϵ-caprolactone)/epoxy blends. *Compos. Part A Appl. Sci. Manuf.* **99**, 129–138 (2017).
48. S. M. S. R. B. Jony, M. Thapa, Repeatable self-healing of thermosetting fiber reinforced polymer composites with thermoplastic healant. *Smart Mater. Struct.* **28**, 025037 (2019).
49. W. H. Martin, J. S. Turicek, J. F. Patrick, Integrated damage sensing and self-healing in polymers and composites: Progress and opportunities. *J. Intell. Mater. Syst. Struct.* **36**, e1045389X251346315 (2025).
50. S. Meure, D. Y. Wu, S. Furman, Polyethylene-co-methacrylic acid healing agents for mendable epoxy resins. *Acta Mater.* **57**, 4312–4320 (2009).
51. S. Meure, D. Y. Wu, S. A. Furman, FTIR study of bonding between a thermoplastic healing agent and a mendable epoxy resin. *Vib. Spectrosc.* **52**, 10–15 (2010).
52. S. Meure *et al*., Confirmation of the healing mechanism in a mendable EMAA-epoxy resin. *Eur. Polym. J.* **48**, 524–531 (2012).
53. A. D. Snyder, J. S. Turicek, C. E. Diesendruck, R. J. Varley, J. F. Patrick, Unraveling chemical and rheological mechanisms of self-healing with EMAA thermoplastics in fiber-reinforced epoxy composites. *Compos. Part A Appl. Sci. Manuf.* **185**, 108271 (2024).
54. K. Pingkarawat, C. Dell'Olio, R. J. Varley, A. P. Mouritz, Poly(ethylene-co-methacrylic acid) (EMAA) as an efficient healing agent for high performance epoxy networks using diglycidyl ether of bisphenol A (DGEBA). *Polymer* **92**, 153–163 (2016).
55. J. S. Turicek, A. D. Snyder, K. B. Nakshatrala, J. F. Patrick, Topological effects of 3D-printed copolymer interlayers on toughening and in situ self-healing in laminated fiber-composites. *Compos. Sci. Technol.* **240**, 110073 (2023).
56. S. M. B. Jony, S. Roy, Fracture resistance of in-situ healed CFRP composite using thermoplastic healants. *Mater. Today Commun.* **24**, 101067 (2020).
57. Q. Ouyang, L. Liu, Z. Wu, Electrothermally self-healing delamination cracks in carbon/epoxy composites using sandwich and tough carbon nanotube/copolymer interleaves. *Polymers* **14**, 4313 (2022).
58. J. S. Turicek, V. Kamala, K. B. Nakshatrala, G. Haikal, J. F. Patrick, Tailoring interlaminar shear and mode-I fracture behavior in fiber-composites via soft self-healing thermoplastic inclusions. *Compos. Part A Appl. Sci. Manuf.* **194**, 108803 (2025).
59. K. Pingkarawat, C. H. Wang, R. J. Varley, A. P. Mouritz, Self-healing of delamination cracks in mendable epoxy matrix laminates using poly[ethylene-co-(methacrylic acid)] thermoplastic. *Compos. Part A Appl. Sci. Manuf.* **43**, 1301–1307 (2012).
60. K. Pingkarawat, C. H. Wang, R. J. Varley, A. P. Mouritz, Self-healing of delamination fatigue cracks in carbon fibre-epoxy laminate using mendable thermoplastic. *J. Mater. Sci.* **47**, 4449–4456 (2012).
61. K. Pingkarawat, C. Dell'Olio, R. J. Varley, A. P. Mouritz, An efficient healing agent for high temperature epoxy composites based upon tetra-glycidyl diamino diphenyl methane. *Compos. Part A Appl. Sci. Manuf.* **78**, 201–210 (2015).
62. S. Meure, S. Furman, S. Khor, Poly[ethylene-co-(methacrylic acid)] healing agents for mendable carbon fiber laminates. *Macromol. Mater. Eng.* **295**, 420–424 (2010).
63. ASTM International, *D5528/D5528M-21: Standard Test Method for Mode I Interlaminar Fracture Toughness of Unidirectional Fiber-Reinforced Polymer Matrix Composites* (2022).
64. J. F. Patrick *et al*., Continuous self-healing life cycle in vascularized structural composites. *Adv. Mater.* **26**, 4302–4308 (2014).
65. K. R. Hart *et al*., Repeated healing of delamination damage in vascular composites by pressurized delivery of reactive agents. *Compos. Sci. Technol.* **151**, 1–9 (2017).
66. United States. Department of Transportation. Bureau of Transportation Statistics, Average age of automobiles and trucks in operation in the united states (2023). https://www.bts.gov/content/average-age-automobiles-and-trucks-operation-united-states. Accessed 18 July 2025.
67. R. H. Wiser, M. Bolinger, Benchmarking anticipated wind project lifetimes: Results from a survey of U.S. wind industry professionals, Energy markets & policy (2019). https://emp.lbl.gov/publications/benchmarking-anticipated-wind-project. Accessed 18 July 2025.
68. United States. Department of Transportation. Bureau of Transportation Statistics, Average age of aircraft 2018, Bureau of transportation statistics (2018). https://www.bts.gov/content/average-age-aircraft. Accessed 18 July 2025.
69. R. D. Trunkey *et al*., Costs of submarine maintenance at public and private shipyards, Congressional budget office (2019). https://www.cbo.gov/publication/55032. Accessed 18 July 2025.
70. Z. P. Bažant, Size effect on structural strength: A review. *Arch. Appl. Mech.* **69**, 703–725 (1999).
71. F. M. Monticeli, M. Y. Pitanga, M. O. H. Cioffi, H. J. C. Voorwald, Mode I and mode II delamination of carbon/glass/epoxy hybrid composite: A statistics-based analysis. *Polym. Compos.* **42**, 3857–3869 (2021).
72. A. Argüelles, P. Coronado, A. F. Canteli, J. Viña, J. Bonhomme, Using a statistical model for the analysis of the influence of the type of matrix carbon-epoxy composites on the fatigue delamination under modes I and II of fracture. *Int. J. Fatigue* **56**, 54–59 (2013).
73. Y. Li, M. Zhou, Prediction of fracture toughness scatter of composite materials. *Comput. Mater. Sci.* **116**, 44–51 (2016).
74. R. Jiang, D. N. P. Murthy, A study of Weibull shape parameter: Properties and significance. *Reliab. Eng. Syst. Safety* **96**, 1619–1626 (2011).
75. National Aviation Academy, The different types of aviation maintenance checks (2020). https://www.naa.edu/types-of-aviation-maintenance-checks/. Accessed 16 March 2025.
76. T. v. d. Weide, Q. Deng, B. F. Santos, Robust long-term aircraft heavy maintenance check scheduling optimization under uncertainty. *Comput. Oper. Res.* **141**, 105667 (2022).
77. R. V. R. S. Ca Aubin, P. R. Buskohl, Autonomous material systems. *MRS Bull.* **49**, 1070–1078 (2024).
78. S. Hashemi, A. J. Kinloch, J. G. Williams, Corrections needed in double-cantilever beam tests for assessing the interlaminar failure of fibre-composites. *J. Mater. Sci. Lett.* **8**, 125–129 (1989).
79. J. S. Turicek, Z. J. Phillips, K. B. Nakshatrala, J. F. Patrick, Self-healing for the long haul: In situ automation delivers century-scale fracture recovery in structural composites. Zenodo. https://zenodo.org/records/17845142. Deposited 18 December 2025.

Supporting Information

Self-healing for the long haul: In situ automation delivers century-scale fracture recovery in structural composites

Jack S. Turicek, Zachary J. Phillips, Kalyana B. Nakshatrala, and Jason F. Patrick

S1. Automated Experimental Evaluation

The test setup shown in **Figure S1a** consists of a double cantilever beam (DCB) specimen gripped in an electromechanical load frame that is connected to a digital multimeter (DMM), which monitors and communicates the voltage outputs from the test frame via a Python code. A power supply is wired to the embedded heaters in the DCB sample to provide the electrical energy required for *in situ* Joule heating, while an overhead IR camera monitors the top surface temperature. Fig. S1b shows the electrical connections that enable the DMM to send digital signals to the load frame to automatically start/stop loading and to also monitor the voltage outputs from the load frame, which correspond to load or displacement. A relay switch (8-channels 5V, SainSmart) operates between the load frame and the DMM to alternate between reading load or displacement, as only one output can be read by the DMM at any given time. The real-time graphic user interface (GUI) (Fig. S1c) features a dashboard to monitor the automated test progression including the cycle count, electrical input from the power supply to the resistive heaters, DCB top surface temperature via IR camera, and the mechanical force versus displacement behavior. The GUI also features numerical inputs to adjust the virgin unload curve offset/rate (see Section S2) if the crack deviates from the prescribed 50 mm of propagation during automated testing.

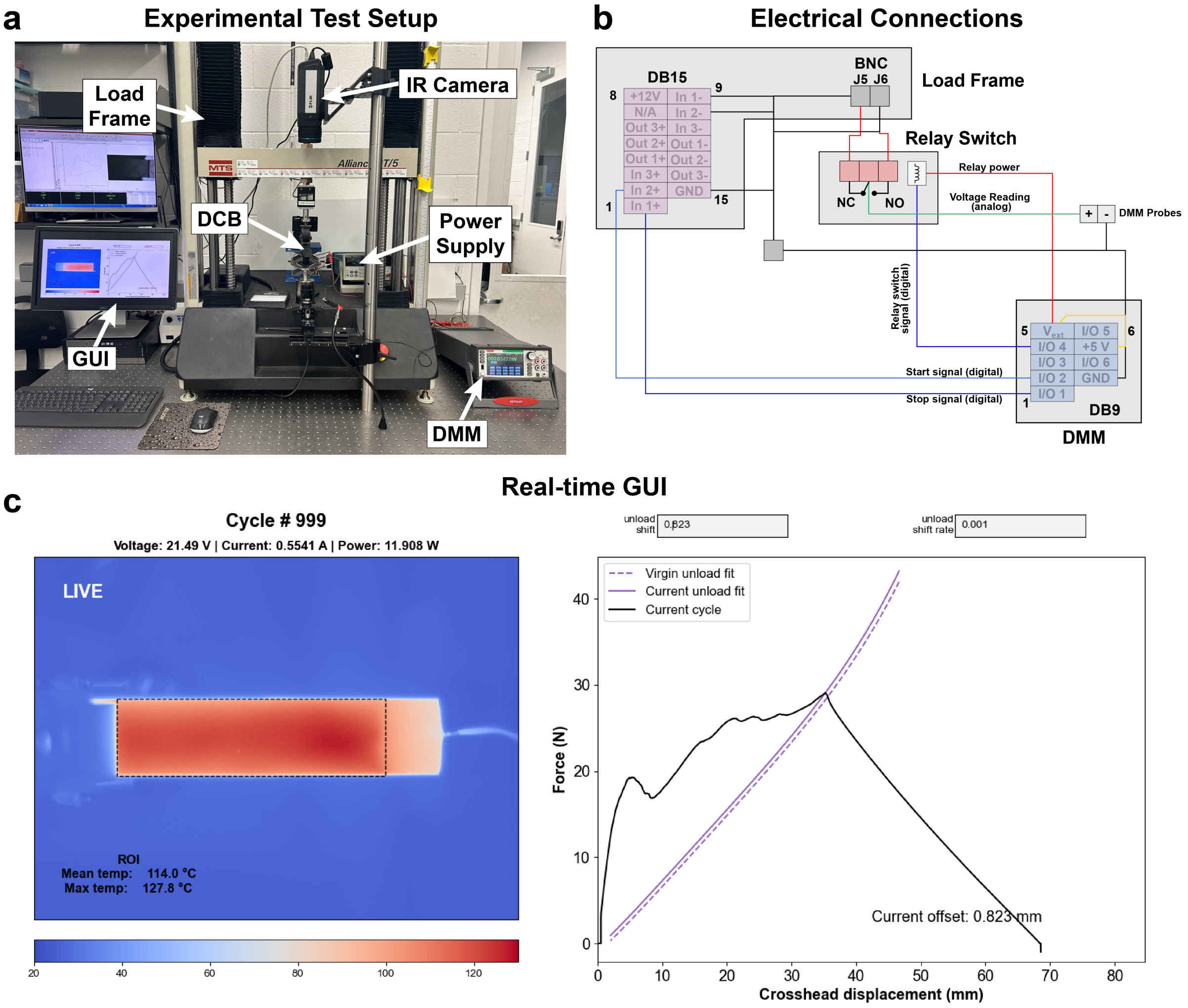

Fig. S1. Automated Experimental Hardware/Software Integration a Experimental test setup and equipment. **b** Electrical connections between electromechanical load frame and digital multimeter (DMM). **c** Real-time GUI to input/monitor test parameters during automated testing.

S2. Automated Unloading Protocol

To automate fracture/heal cycling it is necessary to terminate tensile loading (i.e., stop applying opening displacement) and begin unloading the specimen when the propagating midplane delamination reaches the designated crack length (Δa) of 50 mm. For manual fracture tests, this is accomplished by visually monitoring the bottom surface of the translucent glass-reinforced composite (via a high-resolution 4k webcam) and human intervention at $\Delta \mathrm{a} = 50$ mm. However, for automated fracture testing, the slope of the unload curve from the first virgin fracture cycle (performed manually) is used to trigger unloading for subsequent cycles, as the elastically deformed DCB exhibits the same stiffness/compliance when the crack length is identical.

The details of this automated unload procedure are as follows: once the manual virgin fracture cycle has been performed, a 4th order polynomial is fit to the virgin unload curve that provides a deterministic equation to trigger unloading. While beam theory predicts a cubic response, a 4th order polynomial fit is required to capture the rapid drop in load that occurs at the start of unloading. The fitted unload curve is then shifted in the negative displacement direction (i.e., trigger unloading slightly earlier) to account for any additional crack propagation that occurs during unloading, which is typically minor (1-5%) relative to the 50 mm delamination. This shift in the negative x-direction is manually input via the GUI during the test and programmed to automatically shift an additional amount per cycle (typically -0.001 mm/cycle) to account for the slight, yet unavoidable evolution of the terminating crack front throughout successive cycles. As a subsequent (post-virgin) fracture test progresses, the crosshead continues to load the DCB while the force-displacement curve is traced (**Figure S2a**) (using the voltage outputs read by the DMM) until the current heal cycle force vs. displacement (P_{heal} vs. δ) response crosses over the shifted virgin unload polynomial fit curve (i.e., $P_{\mathrm{heal}}(\delta) < P_{\mathrm{virgin}}(\delta)$), as shown in Fig. S2b. At this point, the load frame is signaled to unload (Fig. S2c) until zero crosshead displacement is reached. The accuracy of this automated unloading technique can be visually discerned in the nearly collinear nature of the overlaid unload curves in Fig. S2d, and also in the extended (i.e., 1,000 cycle) tests from Fig. 3b (in the main text).

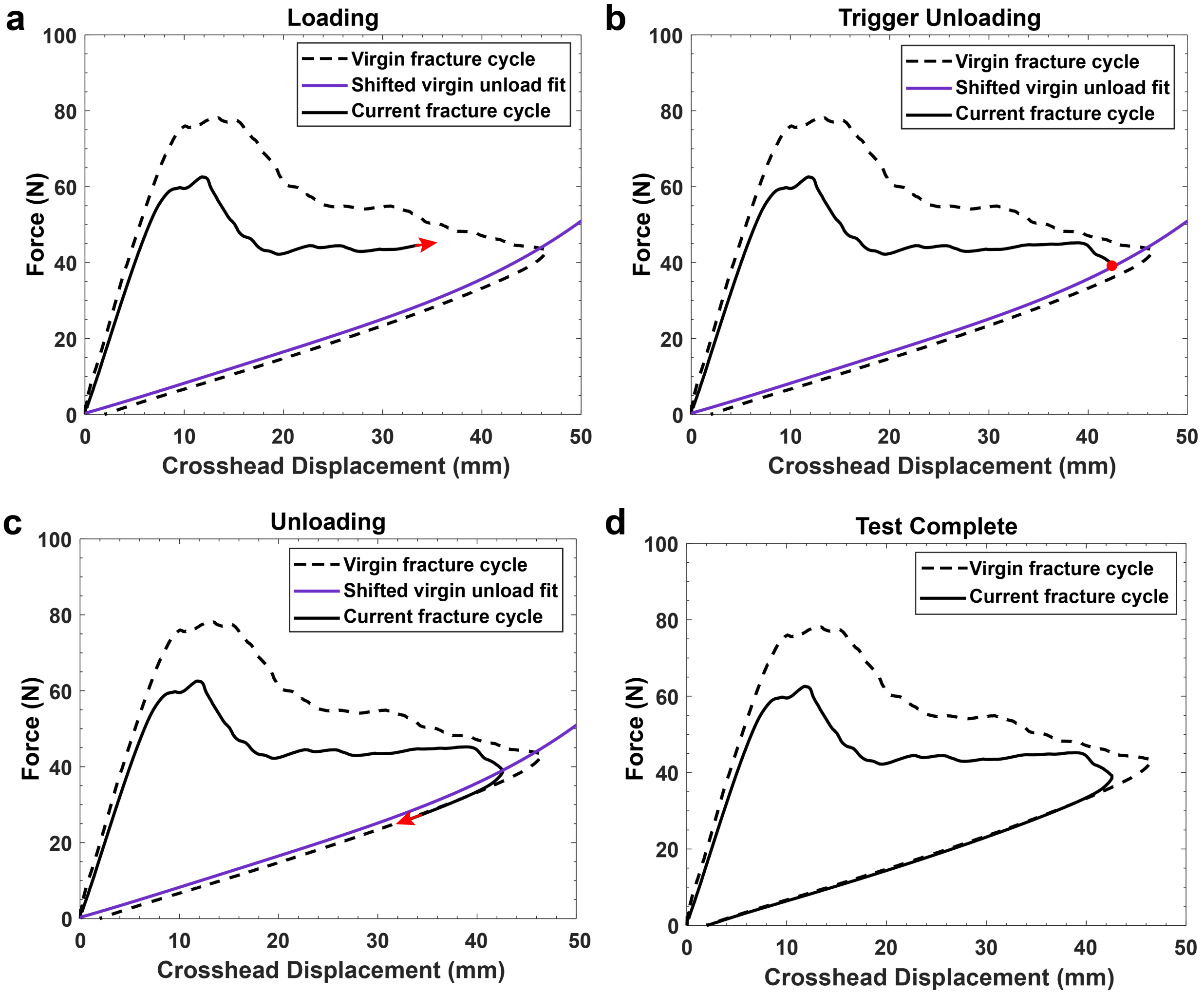

Fig. S2. Automated Unloading Procedure. Post-heal force versus displacement behavior during automated fracture cycling that depicts: **a** initial reloading, **b** reaching the shifted virgin unload curve fit, **c** triggering unloading to zero crosshead displacement, and **d** overlaid load/unload versus displacement curves.